China Ocean Eng., 2022, Vol. 36, No. 4, P. 614–628
DOI: https://doi.org/10.1007/s13344-022-0054-3, ISSN 0890-5487
http://www.chinaoceanengin.cn/ E-mail: coe@nhri.cn

Stochastic Failure Analysis of Reinforced Thermoplastic Pipes Under Axial Loading and Internal Pressure

WANG Yang-yang[a, b], LOU Min[a, b, *], WANG Yu[a, b], WU Wu-gang[c], YANG Feng[d]

[a] School of Petroleum Engineering, China University of Petroleum (East China), Qingdao 266580, China

[b] Key Laboratory of Unconventional Oil & Gas Development (China University of Petroleum (East China)), Ministry of Education, Qingdao 266580, China

[c] Kunming Shipborne Equipment Research and Test Center, China Shipbuilding Industry Corporation, Kunming 650051, China

[d] Cangzhou Mingzhu Plastic Co., Ltd., Cangzhou 061000, China

Received March 5, 2022; revised June 30, 2022; accepted July 26, 2022

Abstract

This study explores how parametric uncertainties in the production affect failure tensile loads of reinforced thermoplastic pipes (RTPs) under combined loading conditions. The stress distributions in RTPs are examined with three-dimensional (3D) elasticity theory, and the analytical micromechanics of composites are evaluated. To evaluate the failure mechanisms for RTPs, 3D Hashin–Yeh failure criteria are combined with the damage evolution model to establish a progressive failure model. The theoretical model has been validated through numerical simulations and axial tensile tests data. To analyze how randomness of relevant parameters affects the first-ply failure (FPF) tensile load and final failure (FF) tensile load in RTPs, many samples are produced with the Monte–Carlo approach. The stochastic analysis results are statistically evaluated through the Weibull probability density distribution function. For the randomness of production parameters, the failure tensile load of RTPs fluctuates near the mean value. As the ply number at the reinforced layer increases, the dispersion of failure tensile load increases, with a high probability that the FPF tensile load of RTPs is lower than the mean value.

Key words: reinforced thermoplastic pipes, micromechanics evaluation, progressive failure, stochastic analysis

Citation: Wang, Y. Y., Lou, M., Wang, Y., Wu, W. G., Yang, F., 2022. Stochastic failure analysis of reinforced thermoplastic pipes under axial loading and internal pressure. China Ocean Eng., 36(4): 614–628, doi: https://doi.org/10.1007/s13344-022-0054-3

1 Introduction

Reinforced thermoplastic pipes (RTPs), commonly used in ocean engineering, are widely used for diverse applications due to their distinctive features, such as anti-corrosion and high flexibility, which ensure that these pipes can be easily transported, installed, and operated (Bai et al., 2014; Wang et al., 2020; Lou et al., 2020; Reis et al., 2017; Toh et al., 2018). The reinforced layer with the sandwich-structure pipe is a special composite composed of two materials. The properties of the composite contribute to the overall structure performance. Therefore, the micromechanics analysis of composite laminates and the accurate prediction of their mechanical parameters are critical. RTPs can be alternatives of metal pipelines for traditional offshore applications. The pipes are exposed to harsh environments. Therefore, developing advanced methods for evaluating the load-bearing capacity for RTPs under different loading conditions is critical (Bakar et al., 2021; Yu et al., 2017; Liu and Wang, 2019a; Wang et al., 2021a, 2021b).

Multiple models have been developed to predict the response of composite cylinders to varying loads. Bai et al. (Bai and Bai, 2014; Bai et al., 2015) investigated the stress distribution of RTPs under various loading conditions through a combination of theoretical analyses, numerical simulations, and experimental studies. Xin et al. (2019) proposed analytical and numerical homogenisation approaches for simulating the macroscopic characteristics in composite lamina to establish an excellent reference for the structural design of fibre-reinforced composite structures. According to Sun et al. (2014a, 2014b), in cylindrically orthotropic composite risers, homogenised elastic constants can be determined using force deformation equivalence and considering stress and strain distribution at each layer. Based on the results of Sun et al., Liu et al. (2021a, 2021b) presented a theoretical model for forecasting RTP failure load subject to axial loads by using the existing homogenisation method

Foundation item: The study was financially supported by the National Natural Science Foundation of China (Grant No. U2006226] and the National Key Research and Development Program of China (Grant No. 2016YFC0303800).

*Corresponding author. E-mail: shidaloumin@163.com

with the nonlinear stiffness degradation model. Betts et al. (2019) studied five filament-wound composite pipe samples with uniaxial compression. The analytical model constructed with the current approach concerning composite flat plates was adopted to verify the results during the experiment, which proved that pipe strength augmented with a decrease in the diameter-thickness ratio. Xing et al. (2015) developed elasticity theory with anisotropy by studying the deformation and stress of a thick filament-wound composite cylinder in a multiangle winding pattern subject to axial loading and internal and external pressures.

For RTP, predicting the progressive damage during loading is challenging due to anisotropy in the composite material. Progressive failure has been studied extensively. Maimí et al. (2007) presented the progressive damage model to simulate damage evolution in composite materials. Hashin (Hashin, 1981; Hashin and Rotem, 1973) and Yeh (Yeh and Chern, 1998; Yeh and Kim, 1994) studied the distinct failure models of composite laminates and proposed failure criteria under various failure modes. The failure criteria of Hashin and Yeh were further studied in the analysis of composite laminate failure, and their results conformed to experimental results (Chen et al., 2017, 2018; He et al., 2019). Thus, the Hashin–Yeh failure criteria are typically used for the progressive damage analysis on composite materials. Rafiee (2013) conducted experimental studies on the fibre-reinforced composite pipes of various sizes for predicting longitudinal and apparent hoop tensile strengths. Gemi (2018) conducted low-velocity tests on three composite pipes, observed the results through scanning electron microscopy, and established a systematic experimental approach to evaluate composite pipe failure.

Studies concerning composite pipe-related mechanical performance have been mostly performed using the deterministic research method. However, design parameters, such as the winding angle and fibre volume content, exhibit randomness due to uncertainty during composite production. Thus, the randomness of design parameters must be considered to precisely predict the mechanical properties of composite pipelines. Limited studies have been performed to examine the mechanical properties of RTPs (Rafiee et al., 2015b). In this study, the stress distribution of RTPs under combined axial loading and internal pressure were analyzed by using 3D elasticity theory, and the analytical micromechanics of the composites were evaluated. In consideration the effect of temperature, the 3D Hashin−Yeh failure criterion was combined with the damage evolution model to establish the progressive failure model. The theoretical model was tested through numerical simulations and axial tensile test data. With considering the parameter randomness of the fibre content and winding angle at the reinforced layer, the Monte–Carlo approach was utilized to generate adequate samples. Tensile failure loads were randomly analyzed with the progressive failure model, and stochastic analysis results were statistically assessed using the Weibull probability density distribution function.

2 Theoretical analysis

RTPs exhibit multiple winding angle filament-wound structures, and the structure of RTPs is shown in Fig. 1. Both liner and outer coating layers are high-density polyethylene (HDPE). The reinforced layer comprised fibreglass inserted into an HDPE matrix wrapped around the inner liner at a specific angle (such as the winding angle) with ply numbers. The alternate-ply layer served as the orthotropic layer. RTPs were under axial loading, and the effects of internal pressure and temperature were considered. Stress analyses and failure assessment were performed on RTPs.

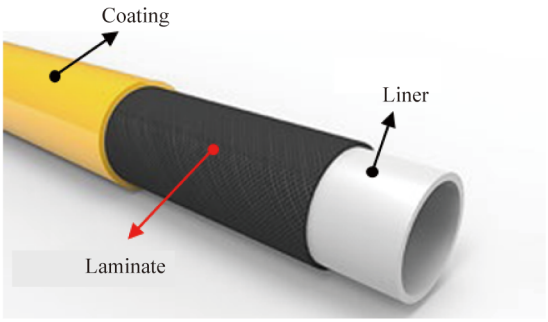

Fig. 1. Structure of RTPs.

2.1 Theoretical model of RTP

For laminated structures in RTPs containing N layers, the principal axis in the single-layer material is inconsistent with the coordinate system of the pipe direction. Thus, the cylindrical coordinate system is set as (z, θ, r), and the associated material coordinate system at the tap layer is set as (1, 2, 3) with α denoting the winding angle in directions 1 and z (Fig. 2).

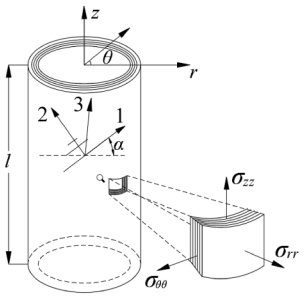

(1,2,3): Local material coordinate system
(z,θ,r): Cylindrical coordinate system

Fig. 2. Coordinate systems for RTPs.

The adjacent layers of RTPs are completely bonded, and the materials of each layer are uniform and continuous with no manufacturing defects. When RTPs are under axisymmetric loads, including internal pressure q_a, axial force T_z, deformation occurs in three directions. The relevant radial, annular, and axial displacements of RTPs are $u(r)$, v (r, z), and $w(z)$, respectively. The strain-related geometric equations

can be presented as follows:

$$\begin{cases} \varepsilon_r = \dfrac{\partial u}{\partial r},\ \gamma_{\theta r} = \dfrac{\partial v}{\partial r} - \dfrac{v}{r} = 0 \\ \varepsilon_\theta = \dfrac{u}{r},\ \gamma_{\theta z} = \dfrac{\partial v}{\partial z} \\ \varepsilon_z = \dfrac{\partial w}{\partial z} = \varepsilon_0,\ \gamma_{zr} = 0 \end{cases} \tag{1}$$

where ε_r, ε_θ, ε_z, $\gamma_{\theta r}$, $\gamma_{\theta z}$, and γ_{zr} denote the strain components.

In accordance with the geometric conditions in RTPs, the equilibrium equation of layers k = 1, 2, ⋯, N can be expressed as follows:

$$\begin{cases} \dfrac{\partial \sigma_r^{(k)}}{\partial r} + \dfrac{\sigma_r^{(k)} - \sigma_\theta^{(k)}}{r} = 0 \\ \dfrac{\partial \tau_{r\theta}^{(k)}}{\partial r} + \dfrac{2\tau_{r\theta}^{(k)}}{r} = 0 \\ \dfrac{\partial \tau_{zr}^{(k)}}{\partial r} + \dfrac{\tau_{zr}^{(k)}}{r} = 0 \end{cases} \tag{2}$$

The positive axial stress–strain relation at each layer in the reinforced layer of the cylindrical coordinate system is given as follows:

$$\begin{bmatrix} \sigma_z^{(k)} \\ \sigma_\theta^{(k)} \\ \sigma_r^{(k)} \\ \tau_{\theta r}^{(k)} \\ \tau_{rz}^{(k)} \\ \tau_{z\theta}^{(k)} \end{bmatrix} = \boldsymbol{C}^{(k)} \begin{bmatrix} \varepsilon_r^{(k)} \\ \varepsilon_\theta^{(k)} \\ \varepsilon_z^{(k)} \\ \gamma_{\theta z}^{(k)} \\ \gamma_{rz}^{(k)} \\ \gamma_{r\theta}^{(k)} \end{bmatrix} = \begin{bmatrix} \overline{C}_{11}^{(k)} & \overline{C}_{12}^{(k)} & \overline{C}_{13}^{(k)} & 0 & 0 & \overline{C}_{16}^{(k)} \\ \overline{C}_{21}^{(k)} & \overline{C}_{22}^{(k)} & \overline{C}_{23}^{(k)} & 0 & 0 & \overline{C}_{26}^{(k)} \\ \overline{C}_{31}^{(k)} & \overline{C}_{32}^{(k)} & \overline{C}_{33}^{(k)} & 0 & 0 & \overline{C}_{36}^{(k)} \\ 0 & 0 & 0 & \overline{C}_{44}^{(k)} & \overline{C}_{45}^{(k)} & 0 \\ 0 & 0 & 0 & \overline{C}_{54}^{(k)} & \overline{C}_{55}^{(k)} & 0 \\ \overline{C}_{61}^{(k)} & \overline{C}_{62}^{(k)} & \overline{C}_{63}^{(k)} & 0 & 0 & \overline{C}_{66}^{(k)} \end{bmatrix} \begin{bmatrix} \varepsilon_z^{(k)} \\ \varepsilon_\theta^{(k)} \\ \varepsilon_r^{(k)} \\ \gamma_{\theta r}^{(k)} \\ \gamma_{rz}^{(k)} \\ \gamma_{z\theta}^{(k)} \end{bmatrix} \tag{3}$$

where $\boldsymbol{C}^{(k)}$ refers to the stiffness compliance at the k-th layer.

In accordance with the conservation of strain-related energy and stress-strain relationship, the stiffness matrix for RTPs in the cylindrical coordinate system is measured with the formula (Xing et al., 2015):

$$\boldsymbol{C}^{(k)} = \boldsymbol{T}_\varepsilon{}^{\mathrm{T}} \boldsymbol{C} \boldsymbol{T}_\varepsilon, \tag{4}$$

where $\boldsymbol{T}_\varepsilon$ is the coordinate transformation matrix with the following specific expression:

$$\boldsymbol{T}_\varepsilon = \begin{bmatrix} m^2 & n^2 & 0 & 0 & 0 & mn \\ n^2 & m^2 & 0 & 0 & 0 & -mn \\ 0 & 0 & 1 & 0 & 0 & 0 \\ 0 & 0 & 0 & m & -n & 0 \\ 0 & 0 & 0 & n & -m & 0 \\ -2mn & 2mn & 0 & 0 & 0 & m^2 - n^2 \end{bmatrix} \tag{5}$$

where $m = \cos\alpha$ and $n = \sin\alpha$.

Because the thermal expansion coefficient along the fibre direction is substantially smaller than the transverse thermal expansion coefficient, the thermal gradient in the RTPs structure can considerably affect the stress distribution of the structure. The temperature distribution and the resulting thermal stress should be considered in the design of RTPs (Bakaiyan et al., 2009). The stress–strain relationship for RTPs in cylindrical coordinates is expressed as follows:

$$\begin{cases} \sigma_z^{(k)} + \xi_z^{(k)} \Delta T = \overline{C}_{11}^{(k)} \varepsilon_z^{(k)} + \overline{C}_{12}^{(k)} \varepsilon_\theta^{(k)} + \overline{C}_{13}^{(k)} \varepsilon_r^{(k)} + \overline{C}_{16}^{(k)} \gamma_{z\theta}^{(k)} \\ \sigma_\theta^{(k)} + \xi_\theta^{(k)} \Delta T = \overline{C}_{21}^{(k)} \varepsilon_z^{(k)} + \overline{C}_{22}^{(k)} \varepsilon_\theta^{(k)} + \overline{C}_{23}^{(k)} \varepsilon_r^{(k)} + \overline{C}_{26}^{(k)} \gamma_{z\theta}^{(k)} \\ \sigma_r^{(k)} + \xi_r^{(k)} \Delta T = \overline{C}_{31}^{(k)} \varepsilon_z^{(k)} + \overline{C}_{32}^{(k)} \varepsilon_\theta^{(k)} + \overline{C}_{33}^{(k)} \varepsilon_r^{(k)} + \overline{C}_{36}^{(k)} \gamma_{z\theta}^{(k)} \\ \tau_{\theta r}^{(k)} = \overline{C}_{44}^{(k)} \gamma_{\theta r}^{(k)} + \overline{C}_{45}^{(k)} \gamma_{zr}^{(k)} \\ \tau_{zr}^{(k)} = \overline{C}_{54}^{(k)} \gamma_{\theta r}^{(k)} + \overline{C}_{55}^{(k)} \gamma_{zr}^{(k)} \\ \tau_{z\theta}^{(k)} + \xi_{z\theta}^{(k)} \Delta T = \overline{C}_{61}^{(k)} \varepsilon_z^{(k)} + \overline{C}_{62}^{(k)} \varepsilon_\theta^{(k)} + \overline{C}_{63}^{(k)} \varepsilon_r^{(k)} + \overline{C}_{66}^{(k)} \gamma_{z\theta}^{(k)} \end{cases} \tag{6a}$$

where the expression of $\xi^{(k)}$ is as follows:

$$\begin{cases} \xi_z^{(k)} = \overline{C}_{11}^{(k)} \alpha_z^{(k)} + \overline{C}_{12}^{(k)} \alpha_\theta^{(k)} + \overline{C}_{13}^{(k)} \alpha_r^{(k)} + 2\overline{C}_{16}^{(k)} \alpha_{z\theta}^{(k)} \\ \xi_\theta^{(k)} = \overline{C}_{21}^{(k)} \alpha_z^{(k)} + \overline{C}_{22}^{(k)} \alpha_\theta^{(k)} + \overline{C}_{23}^{(k)} \alpha_r^{(k)} + 2\overline{C}_{26}^{(k)} \alpha_{z\theta}^{(k)} \\ \xi_r^{(k)} = \overline{C}_{31}^{(k)} \alpha_z^{(k)} + \overline{C}_{32}^{(k)} \alpha_\theta^{(k)} + \overline{C}_{33}^{(k)} \alpha_r^{(k)} + 2\overline{C}_{36}^{(k)} \alpha_{z\theta}^{(k)} \\ \xi_{z\theta}^{(k)} = \overline{C}_{61}^{(k)} \alpha_z^{(k)} + \overline{C}_{62}^{(k)} \alpha_\theta^{(k)} + \overline{C}_{63}^{(k)} \alpha_r^{(k)} + 2\overline{C}_{66}^{(k)} \alpha_{z\theta}^{(k)} \end{cases} \tag{6b}$$

where $\overline{C}_{ij}^{(k)}$ represents the stiffness constant, and $\alpha_{ij}{}^{(k)}$ is the thermal expansion coefficient. ΔT denotes the temperature difference.

Subject to axisymmetric internal-to-external temperature difference, ΔT is determined through radial temperature distribution $T(r)$ and reference temperature T_{ref}, as follows:

$$\Delta T = T(r) - T_{\mathrm{ref}}. \tag{7}$$

The radial temperature distribution of RTPs is as follows (Hastie et al., 2019):

$$T(r) = \frac{T^{(k)} - T^{(k-1)}}{\ln \dfrac{r^{(k)}}{r^{(k-1)}}} \ln \frac{r}{r^{(k)}} + \frac{\lambda_r^{(k)} T^{(k-1)} \ln \dfrac{r^{(k+1)}}{r^{(k)}} + \lambda_r^{(k+1)} T^{(k+1)} \ln \dfrac{r^{(k)}}{r^{(k-1)}}}{\lambda_r^{(k)} \ln \dfrac{r^{(k+1)}}{r^{(k)}} + \lambda_r^{(k+1)} \ln \dfrac{r^{(k)}}{r^{(k-1)}}} \tag{8}$$

where λ_r is the radial thermal conductivity.

In accordance with the equilibrium and strain geometry equations, general expressions for axial and annular displacements are obtained using the following equations:

$$w = \varepsilon_0 z,\ v = Hrz. \tag{9}$$

The radial displacement equation is calculated as follows:

$$\frac{\mathrm{d}^2u^{(k)}}{\mathrm{d}r^2}+\frac{1}{r}\frac{\partial u^{(k)}}{\partial r}-\frac{\overline{C}_{22}^{(i)}}{\overline{C}_{33}^{(k)}}\frac{u^{(k)}}{r^2}=\frac{\overline{C}_{12}^{(k)}-\overline{C}_{13}^{(k)}}{2\overline{C}_{33}^{(k)}}\frac{\varepsilon_0}{r}-\frac{2\overline{C}_{36}^{(k)}-\overline{C}_{26}^{(k)}}{\overline{C}_{33}^{(k)}}H. \tag{10}$$

When $s_k=\sqrt{\overline{C}_{22}^{(k)}\Big/\overline{C}_{33}^{(k)}}$ is determined, expressions for stress and radial displacement vary with s_k.

When $s_k=1$:

$$\begin{cases}
\sigma_{zz}|_{r=r_{k+1}}=\left(\overline{C}_{12}^{k}+\overline{C}_{13}^{k}\right)D_1^{(k)}+\left(\overline{C}_{12}^{k}-\overline{C}_{13}^{k}\right)D_2^{(k)}r_{k+1}^{-2}-\left[\dfrac{2\left(\overline{C}_{12}^{(k)}+\overline{C}_{13}^{(k)}\right)\left(2\overline{C}_{36}^{(k)}-\overline{C}_{26}^{(k)}\right)-3\overline{C}_{16}^{(k)}\overline{C}_{33}^{(k)}}{3\overline{C}_{33}^{(k)}}\right]Hr_{k+1}\\
\quad+\varepsilon_0\left[\overline{C}_{11}^{(k)}+\dfrac{\left(\overline{C}_{31}^{(k)}-\overline{C}_{21}^{(k)}\right)\overline{C}_{13}^{(k)}+\left(\overline{C}_{12}^{(k)}+\overline{C}_{13}^{(k)}\right)\left(\overline{C}_{31}^{(k)}-\overline{C}_{21}^{(k)}\right)\ln r_{k+1}}{2\overline{C}_{33}^{(k)}}\right]\\
\sigma_{rr}|_{r=r_{k+1}}=\left(\overline{C}_{33}^{k}+\overline{C}_{32}^{k}\right)D_1^{(k)}+D_2^{(k)}\left(\overline{C}_{32}^{k}\cdot r_{k+1}^{-2}-\overline{C}_{33}^{k}\cdot r_{k+1}^{-2}\right)-\left[\dfrac{\left(\overline{C}_{32}^{(k)}+2\overline{C}_{33}^{(k)}\right)\left(2\overline{C}_{36}^{(k)}-\overline{C}_{26}^{(k)}\right)-3\overline{C}_{36}^{(k)}\overline{C}_{23}^{(k)}}{3\overline{C}_{33}^{(k)}}\right]Hr_{k+1}\\
\quad+\varepsilon_0\left[\dfrac{3\overline{C}_{31}^{(k)}-\overline{C}_{21}^{(k)}}{2}+\dfrac{(\overline{C}_{32}^{(k)}+\overline{C}_{33}^{(k)})(\overline{C}_{31}^{(k)}-\overline{C}_{21}^{(k)})}{2\overline{C}_{33}^{(k)}}\right]\ln r_{k+1}\\
\sigma_{z\theta}\big|_{r=r_{k+1}}=\left(\overline{C}_{62}^{(k)}+\overline{C}_{63}^{(k)}\right)D_1^{(k)}+\left(\overline{C}_{62}^{(k)}-\overline{C}_{63}^{(k)}\right)r_{k+1}^{-2}D_2^{(k)}+\left[\overline{C}_{66}^{(k)}-\dfrac{\left(2\overline{C}_{62}^{(k)}+\overline{C}_{63}^{(k)}\right)\left(2\overline{C}_{36}^{(k)}-\overline{C}_{26}^{(k)}\right)}{3\overline{C}_{33}^{(k)}}\right]Hr_{k+1}\\
\quad+\varepsilon_0\left[\overline{C}_{61}^{(k)}+\dfrac{\left(\overline{C}_{62}^{(k)}+\overline{C}_{63}^{(k)}\right)\left(\overline{C}_{31}^{(k)}-\overline{C}_{21}^{(k)}\right)}{2\overline{C}_{33}^{(k)}}\ln r_{k+1}+\dfrac{\overline{C}_{63}^{(k)}\left(\overline{C}_{31}^{(k)}-\overline{C}_{21}^{(k)}\right)}{2\overline{C}_{33}^{(k)}}\right]\\
u_{rr}|_{r=r_{k+1}}=D_1^{(k)}r_{k+1}+D_2^{(k)}r_{k+1}^{-1}+\dfrac{\overline{C}_{12}^{(k)}-\overline{C}_{13}^{(k)}}{2\overline{C}_{33}^{(k)}}\varepsilon_0 r_{k+1}\ln r_{k+1}-\dfrac{2\overline{C}_{36}^{(k)}-\overline{C}_{26}^{(k)}}{3\overline{C}_{33}^{(k)}}Hr_{k+1}^2
\end{cases} \tag{11}$$

When $s_k=2$:

$$\begin{cases}
\sigma_{zz}|_{r=r_{k+1}}=\left(\overline{C}_{12}^{k}+2\overline{C}_{13}^{k}\right)D_1^{(k)}r_{k+1}+\left(\overline{C}_{12}^{k}-2\overline{C}_{13}^{k}\right)D_2^{(k)}r_{k+1}^{-3}+\varepsilon_0\left[\overline{C}_{11}^{(k)}+\dfrac{\left(\overline{C}_{12}^{(k)}+\overline{C}_{13}^{(k)}\right)\left(\overline{C}_{31}^{(k)}-\overline{C}_{21}^{(k)}\right)}{3\overline{C}_{33}^{(k)}}\right]\\
\quad+\left[\overline{C}_{16}^{k}-\dfrac{\overline{C}_{13}^{k}\left(2\overline{C}_{36}^{(k)}-\overline{C}_{26}^{(k)}\right)}{4\overline{C}_{33}^{(k)}}-\dfrac{\left(\overline{C}_{12}^{(k)}+2\overline{C}_{13}^{(k)}\right)\left(2\overline{C}_{36}^{(k)}-\overline{C}_{26}^{(k)}\right)}{4\overline{C}_{33}^{(k)}}\ln r_{k+1}\right]Hr_{k+1}\\
\sigma_{rr}|_{r=r_{k+1}}=\left(\overline{C}_{32}^{k}+2\overline{C}_{33}^{k}\right)r_{k+1}D_1^{(k)}+D_2^{(k)}\left(\overline{C}_{32}^{k}-2\overline{C}_{33}^{k}\right)r_{k+1}^{-3}+\varepsilon_0\left[\overline{C}_{31}^{(k)}+\dfrac{\left(\overline{C}_{32}^{(k)}+\overline{C}_{33}^{(k)}\right)\left(\overline{C}_{31}^{(k)}-\overline{C}_{21}^{(k)}\right)}{3\overline{C}_{33}^{(k)}}\right]\\
\quad-\left[\dfrac{\left(\overline{C}_{32}^{(k)}+2\overline{C}_{33}^{(k)}\right)\left(2\overline{C}_{36}^{(k)}-\overline{C}_{26}^{(k)}\right)}{4\overline{C}_{33}^{(k)}}\ln r_{k+1}-\dfrac{2\overline{C}_{36}^{(k)}+\overline{C}_{26}^{(k)}}{4}\right]Hr_{k+1}\\
\sigma_{z\theta}\big|_{r=r_{k+1}}=\left(\overline{C}_{62}^{(k)}+2\overline{C}_{63}^{(k)}\right)r_{k+1}D_1^{(k)}+\left(\overline{C}_{62}^{(k)}-2\overline{C}_{63}^{(k)}\right)r_{k+1}^{-3}D_2^{(k)}+\varepsilon_0\left[\overline{C}_{61}^{(k)}+\dfrac{\left(\overline{C}_{62}^{(k)}+\overline{C}_{63}^{(k)}\right)\left(\overline{C}_{31}^{(k)}-\overline{C}_{21}^{(k)}\right)}{3\overline{C}_{33}^{(k)}}\right]\\
\quad+\left[\overline{C}_{66}^{(k)}-\dfrac{\overline{C}_{63}^{(k)}\left(2\overline{C}_{36}^{(k)}-\overline{C}_{26}^{(k)}\right)}{4\overline{C}_{33}^{(k)}}-\dfrac{\left(\overline{C}_{62}^{(k)}+2\overline{C}_{63}^{(k)}\right)\left(2\overline{C}_{36}^{(k)}-\overline{C}_{26}^{(k)}\right)}{4\overline{C}_{33}^{(k)}}\ln r_{k+1}\right]Hr_{k+1}\\
u_{rr}|_{r=r_{k+1}}=D_1^{(k)}r_{k+1}^2+D_2^{(k)}r_{k+1}^{-2}+\dfrac{\overline{C}_{12}^{(k)}-\overline{C}_{13}^{(k)}}{3\overline{C}_{33}^{(k)}}\varepsilon_0 r_{k+1}-\dfrac{2\overline{C}_{36}^{(k)}-\overline{C}_{26}^{(k)}}{4\overline{C}_{33}^{(k)}}Hr_{k+1}^2\ln r_{k+1}
\end{cases} \tag{12}$$

When $s_k \neq 1$ and $s_k \neq 2$:

$$\begin{cases}
\sigma_{zz}|_{r=r_{k+1}} = \left(\overline{C}_{12}^{k} + 2s_k\right) D_1^{(k)} r_{k+1}^{s_k-1} + \left(\overline{C}_{12}^{k} - \overline{C}_{13}^{k} s_k\right) D_2^{(k)} r_{k+1}^{-s_k-1} + \varepsilon_0 \left[\overline{C}_{11}^{(k)} - \dfrac{\left(\overline{C}_{12}^{(k)} + \overline{C}_{13}^{(k)}\right)\left(\overline{C}_{31}^{(k)} - \overline{C}_{21}^{(k)}\right)}{\overline{C}_{33}^{(k)} - \overline{C}_{22}^{(k)}}\right] \\
\quad + \left[\overline{C}_{16}^{k} - \dfrac{\left(\overline{C}_{12}^{(k)} + 2\overline{C}_{13}^{(k)}\right)\left(2\overline{C}_{36}^{(k)} - \overline{C}_{26}^{(k)}\right)}{4\overline{C}_{33}^{(k)} - \overline{C}_{22}^{(k)}}\right] H r_{k+1} \\
\sigma_{rr}|_{r=r_{k+1}} = \left(\overline{C}_{32}^{k} + \overline{C}_{33}^{k} s_k\right) D_1^{(k)} r_{k+1}^{s_k-1} + \left(\overline{C}_{32}^{k} - \overline{C}_{33}^{k} s_k\right) D_2^{(k)} r_{k+1}^{-s_k-1} + \varepsilon_0 \left[\overline{C}_{31}^{(k)} - \dfrac{\left(\overline{C}_{32}^{(k)} + \overline{C}_{33}^{(k)}\right)\left(\overline{C}_{31}^{(k)} - \overline{C}_{21}^{(k)}\right)}{\overline{C}_{33}^{(k)} - \overline{C}_{22}^{(k)}}\right] \\
\quad + \left[\overline{C}_{36}^{(k)} - \dfrac{\left(\overline{C}_{32}^{(k)} + 2\overline{C}_{33}^{(k)}\right)\left(2\overline{C}_{36}^{(k)} - \overline{C}_{26}^{(k)}\right)}{4\overline{C}_{33}^{(k)} - \overline{C}_{22}^{(k)}}\right] H r_{k+1} \\
\sigma_{z\theta}\big|_{r=r_{k+1}} = \left(\overline{C}_{62}^{(k)} + \overline{C}_{63}^{(k)} s_k\right) D_1^{(k)} r_{k+1}^{s_k-1} + \left(\overline{C}_{62}^{(k)} - \overline{C}_{63}^{(k)} s_k\right) D_2^{(k)} r_{k+1}^{-s_k-1} + \varepsilon_0 \left[\overline{C}_{61}^{(k)} - \dfrac{\left(\overline{C}_{62}^{(k)} + \overline{C}_{63}^{(k)}\right)\left(\overline{C}_{31}^{(k)} - \overline{C}_{21}^{(k)}\right)}{\overline{C}_{33}^{(k)} - \overline{C}_{22}^{(k)}}\right] \\
\quad + \left[\overline{C}_{66}^{(k)} - \dfrac{\left(\overline{C}_{62}^{(k)} + 2\overline{C}_{63}^{(k)}\right)\left(2\overline{C}_{36}^{(k)} - \overline{C}_{26}^{(k)}\right)}{4\overline{C}_{33}^{(k)} - \overline{C}_{22}^{(k)}}\right] H r_{k+1} \\
u_{rr}|_{r=r_{k+1}} = D_1^{(k)} r_{k+1}^{s_k} + D_2^{(k)} r_{k+1}^{-s_k} + \dfrac{\overline{C}_{12}^{(k)} - \overline{C}_{13}^{(k)}}{\overline{C}_{22}^{(k)} - \overline{C}_{33}^{(k)}} \varepsilon_0 r_{k+1} - \dfrac{2\overline{C}_{36}^{(k)} - \overline{C}_{26}^{(k)}}{4\overline{C}_{33}^{(k)} - \overline{C}_{22}^{(k)}} H r_{k+1}^2
\end{cases} \tag{13}$$

Integral constants $D_1{}^{(i)}$ and $D_2{}^{(i)}$ are derived under boundary conditions for RTPs and continuity conditions for the radial stress and radial displacement of the interface between neighbouring layers (Wang et al., 2021b):

The boundary condition:

$$\sigma_r^{(1)} = q_a. \tag{14}$$

Continuity conditions:

$$\begin{cases} \sigma_r^{(i)}\big|_{r=r_i} = \sigma_r^{(i+1)}\big|_{r=r_i} \\ u_r^{(i)}\big|_{r=r_i} = u_r^{(i+1)}\big|_{r=r_i}, \ i = 1,2,...,N-1 \end{cases} \tag{15}$$

Axial balance equation:

$$2\pi \sum_{i=1}^{k} \int_{r_{i-1}}^{r_i} \sigma_{zz}^{(i)} r \mathrm{d}r = T_Z + q_a \pi r_0^2 \tag{16}$$

Because $2k+2$ unknowns are available in the displacement function, integral constants are derived. Accordingly, the whole stress and strain fields are calculated.

For N-layered RTPs, $2N+2$ unknown integral constants are available. Thus, the whole stress and strain fields are calculated as follows:

$$\left\{ -q_a \quad 0 \quad \cdots \quad 0 \quad 0 \quad \cdots \quad T_z/\pi + q_a r_0^2 \quad 0 \right\} = \boldsymbol{K} \left\{ D_1^{(1)} \quad D_2^{(1)} \quad \cdots \quad D_1^{(i)} \quad D_2^{(i)} \quad \cdots \quad \varepsilon_0 \quad H \right\} \tag{17}$$

where

$$\boldsymbol{K} = \begin{bmatrix}
K_{1,1} & K_{2,1} & \cdots & 0 & 0 & 0 & 0 & \cdots & 0 & 0 & K_{1,2N+1} & K_{1,2N+2} \\
0 & 0 & \cdots & 0 & 0 & 0 & 0 & \cdots & K_{2,2N-1} & K_{2,2N} & K_{2,2N+1} & K_{2,2N+2} \\
\cdots & \cdots & \cdots & \cdots & \cdots & \cdots & \cdots & \cdots & \cdots & \cdots & \cdots & \cdots \\
0 & 0 & \cdots & K_{2k+1,2k-1} & K_{2k+1,2k} & K_{2k+1,2k+1} & K_{2k+1,2k+2} & \cdots & 0 & 0 & K_{2k+1,2N+1} & K_{2k+1,2N+2} \\
0 & 0 & \cdots & K_{2k+2,2k-1} & K_{2k+2,2k} & K_{2k+2,2k+1} & K_{2k+2,2k+2} & \cdots & 0 & 0 & K_{2k+2,2N+1} & K_{2k+2,2N+2} \\
\cdots & \cdots & \cdots & \cdots & \cdots & \cdots & \cdots & \cdots & \cdots & \cdots & \cdots & \cdots \\
K_{2N+1,1} & K_{2N+1,2} & \cdots & K_{2N+1,2k-1} & K_{2N+1,2k} & K_{2N+1,2k+1} & K_{2N+1,2k+2} & \cdots & K_{2N+1,2N-1} & K_{2N+1,2N} & K_{2N+1,2N+1} & K_{2N+1,2N+2} \\
K_{2N+2,1} & K_{2N+2,2} & \cdots & K_{2N+2,2k-1} & K_{2N+2,2k} & K_{2N+2,2k+1} & K_{2N+2,2k+2} & \cdots & K_{2N+2,2N-1} & K_{2N+2,2N} & K_{2N+2,2N+1} & K_{2N+2,2N+2}
\end{bmatrix} \tag{18}$$

2.2 Analytical micromechanics evaluation

In laminates, the fibre volume content and winding angle are the primary factors affecting the RTP-related mechanical behaviour. Theoretically, the effect of the fibre volume content on mechanical performance and laminate strength was observed according to micromechanics rules. Limited studies have been conducted on laminates composed of the polymer matrix and reinforced fibres by using multi-scale prediction for modulus and ultimate capacity (Xin et al., 2019).

The material parameters for reinforced laminates of HDPE and glass fibre estimated by using various studies are presented in Table 1. The data of Table 1 and the stress-strain relationship for HDPE materials were obtained in the laboratory using the material supplier, assuming that the fibre and HDPE were isotropic materials. The anisotropic elastic constants and ultimate strength parameters of the reinforced laminates were also measured in the laboratory by employing the material supplier. Based on the results, the formulations exhibited sufficient accuracy for research.

Table 1 Material parameters for the sample pipes

	Experimental parameters	Value
Glass fibre	Elastic modulus E_f (GPa)	72
	Poisson's ratio v_f	0.2
	Thermal expansivity α_f (K^{-1})	6.01×10^{-6}
	Thermal conductivity λ_f [W (m·K)]	–
	Tensile strength F_{ft} (MPa)	1834
HDPE	Elastic modulus E_m (MPa)	1200
	Poisson's ratio v_m	0.38
	Ultimate strength σ (MPa)	29
	Thermal expansivity α_m (K^{-1})	120×10^{-6}
	Thermal conductivity λ_m [W (m·K)]	0.49
	Yield stress σ_s (MPa)	19
	Tensile strength F_{mt} (MPa)	30

Thermal expansion coefficients are hypothesised as constants in the temperature scope of this study.

(1) Prediction for engineering constants

Elastic constants for the glass fibre and HDPE and corresponding relative volume contents were introduced to predict elastic constants for composite laminates. The improved rules of mixtures are as follows (Shen et al., 2013; Xin et al., 2019):

$$E_1 = E_f V_f + E_m V_m; \tag{19}$$

$$E_2 = E_3 = \frac{E_f E_m (V_f + \eta_1 V_m)}{E_m V_f + E_f \eta_1 V_m}; \tag{20}$$

$$\eta_1 = \frac{0.2}{1 - v_m}\left[1.1 - \left(\frac{E_m}{E_f}\right)^{0.5} + \frac{3.5E_m}{E_f}\right](1 + 0.22V_f); \tag{21}$$

$$G_{23} = \frac{G_f G_m (V_f + \eta_2 V_m)}{G_m G_f + G_f \eta_2 V_m}; \tag{22}$$

$$\eta_2 = 0.388 - 0.665\left(\frac{E_m}{E_f}\right)^{0.5} + 2.56\frac{E_m}{E_f}. \tag{23}$$

Poisson's ratio v_{21} and shear modulus G_{12} and G_{13} measured with the rules for mixtures disagreed with the experimental results. Therefore, other analysis approaches were used. The monolayer composite material was reduced to series model I and parallel model II, as illustrated in Fig. 3 (Shen et al., 2013).

The formulas used to calculate the elastic constants in different models are as follows:

$$v_{21}^{I} = v_f V_f + v_m V_m; \tag{24}$$

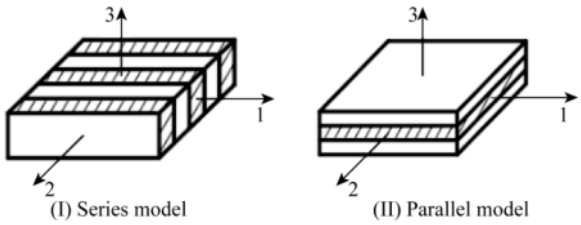

Fig. 3. Simplified model of composite materials.

$$v_{21}^{II} = \frac{v_f E_f V_f + v_m E_m V_m}{E_f V_f + E_m V_m}; \tag{25}$$

$$G_{12}^{I} = G_{13}^{I} = \frac{G_f G_m}{G_m V_f + G_f V_m}; \tag{26}$$

$$G_{12}^{II} = G_{13}^{II} = G_f V_f + G_m V_m. \tag{27}$$

Superscripts I and II correspond to the calculation formulas of various models (Fig. 3).

Because fibres are incompletely parallel, and a lateral contact exists, the contact coefficient C is adopted to denote the contact degree. $C = 0$ suggests the absence of contact, which corresponds to Model I; $C = 1$ represents the transverse complete connection, which corresponds to Model II. Based on overall considerations, the expressions of v_{21}, G_{12}, and G_{13} are obtained as follows:

$$v_{21} = (1 - C)v_{21}^{I} + Cv_{21}^{II}, v_{12} = v_{13} = v_{21}\frac{E_2}{E_1}; \tag{28}$$

$$G_{12} = G_{13} = (1 - C)G_{12}^{I} + CG_{12}^{II}, \tag{29}$$

where C represents the contact coefficient of 0.2 (Shen et al., 2013).

(2) Prediction of ultimate strength

Many factors, such as the strength as well as physical properties of the fibre and matrix, fibre distribution, and volume content, affect the strength of composite materials. The ultimate strength components at fibre-reinforced layers are calculated using the following formulas (Davydenko, 1970, Xin et al., 2019):

$$X_T = F_{ft}\left(V_f + \frac{E_m V_m}{E_f}\right); \tag{30}$$

$$X_C = \begin{cases} 2V_f\sqrt{\dfrac{\beta E_f E_m V_f}{3V_m}}, & \text{in-phase shear mode} \\ \dfrac{\beta G_m}{1 - V_f}, & \text{out-of-phase mode} \end{cases} \tag{31}$$

The longitudinal compressive strength X_C represents the smaller value in in-phase shear and out-of-phase modes.

$$Y_t = Z_T = F_{mt}\left[1 - \sqrt{\frac{4V_v}{\pi(1 - V_f)}}\right]\left[1 + \left(V_f - \sqrt{V_f}\right)\left(1 - \frac{E_m}{E_f}\right)\right]; \tag{32}$$

$$Y_C = Z_C = E_2\varepsilon_{mc}\left[1 - \left(\frac{4V_f}{\pi}\right)^{0.5}\left(1 - \frac{E_m}{E_f}\right)\right]. \tag{33}$$

The in-phase shear strengths X_{12}, X_{13}, and X_{23} were assumed not to be considerably affected by the fibre content. This assumption is based on the experimental observations of Rafiee and Amini (2015). The calculation results of the mathematical model were compared with the experimental results of the material supplier. The comparison results are presented in Tables 2 and 3. According to the calculation results (Tables 2 and 3), the error of numerical and experimental results approached 10%. Therefore, the aforementioned results exhibit adequate accuracy for the research objective.

Table 2 Comparison of elastic constants between the experimental and numerical results

	E_1 (GPa)	E_2 (GPa)	E_3 (GPa)	G_{12} (GPa)	G_{13} (GPa)	G_{23} (GPa)	v_{12}	v_{13}	v_{23}
Experimental solution	28	3.2	3.2	2.7	2.7	1.23	0.034	0.034	0.3
Numerical solution	29.52	3.31	3.31	3.03	3.03	1.24	0.032	0.032	0.37

Table 3 Comparison of the ultimate strength between the experimental and numerical results

	X_T (MPa)	X_C (MPa)	Y_T (MPa)	Z_T (MPa)	Y_C (MPa)	Z_C (MPa)	X_{12} (MPa)	X_{13} (MPa)	X_{23} (MPa)
Experimental solution	829	146	25	25	59	59	18	18	20
Numerical solution	752	145	21	21	55	55	18	18	20

(3) Prediction of thermal expansion coefficients

In addition to the mechanical performance of composite reinforced laminates, their thermal performance was anisotropic. The thermal expansion coefficients of the composite reinforced laminates were assumed to be α_1, α_2, and α_3. The thermal expansion coefficients α_f and α_m of the fibre and matrix were used to predict the thermal expansion coefficients of composite reinforced laminates. The coefficients can be expressed as follows (Shen et al., 2013):

$$\alpha_1 = [V_f\alpha_f E_f + (1 - V_f)\alpha_m E_m]/E_1; \tag{34}$$

$$\alpha_2 = \alpha_3 = (1 + v_m)\alpha_m(1 - V_f) + (1 + v_f)\alpha_f V_f - \alpha_1 v_{12}. \tag{35}$$

where X_T, X_C, Y_T, Y_C, Z_T, Z_C, X_{12}, X_{13}, and X_{23} denote the strength parameters in the reinforced tape.

The finite element software ANSYS Material Designer was used to verify the prediction accuracy of thermal expansion coefficients. ANSYS Material Designer is a powerful tool that replaces expensive experimental testing. Its algorithms are adopted to calculate homogenised material properties according to the known base material properties. In this study, the material models were used on the basis of the representative volume element (RVE). To simulate reinforced layer composites accurately, the random unidirectional composites, which comprised fibres with random variations in the orientation direction, surrounded by a matrix material were selected (Fig. 4). The seed number against which the random fibre directions and mean misalignment angle were generated was defined according to the fibre volume content. The higher were the fibre volume content and the mean misalignment angle, the more difficult was the generation of RVE. Therefore, the angle of misalignment was considered 0.3 for large values of the fibre volume content.

As displayed in Fig. 4, the direction along the fibre is defined as the *X*-direction, and the directions perpendicular to the fibre are the *Y*- and *Z*-directions. The comparison results are presented in Fig. 5.

According to the comparison shown in Fig. 5, the difference between the calculated results of theoretical formulas and the finite element software is small (smaller than 10%). The thermal conductivity of reinforced laminates is nearly the same as that of the matrix material because the conductivity of the fibre thermal is considerably smaller than that of the matrix material.

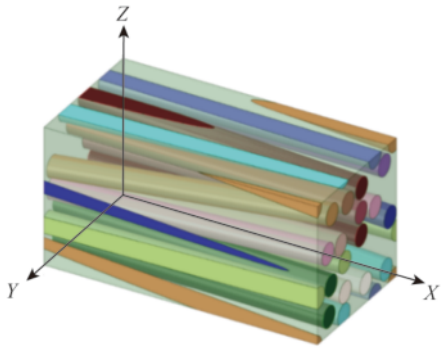

Fig. 4. Random unidirectional composite material.

2.3 Failure criteria

The stress-based failure criterion has been widely used to predict composite structure failure because it is convenient to compute stress components (Rafiee and Torabi, 2018). In the current section, the 3D Hashin–Yeh failure criterion was adopted to predict the damage against fibre-reinforced laminates. Afterwards, Von–Mises criterion (Liu et al., 2021b) was used to evaluate the failure modes for isotropic material. Relevant expressions are presented in Eqs. (36)–(43) (Hashin, 1981; Hashin and Rotem, 1973; Yeh and Chern, 1998).

Von-Mises criterion:

$$(\sigma_1 - \sigma_2)^2 + (\sigma_2 - \sigma_3)^2 + (\sigma_3 - \sigma_1)^2 + 6(\tau_{12}^2 + \tau_{13}^2 + \tau_{23}^2) = 2\sigma_s^2. \tag{36}$$

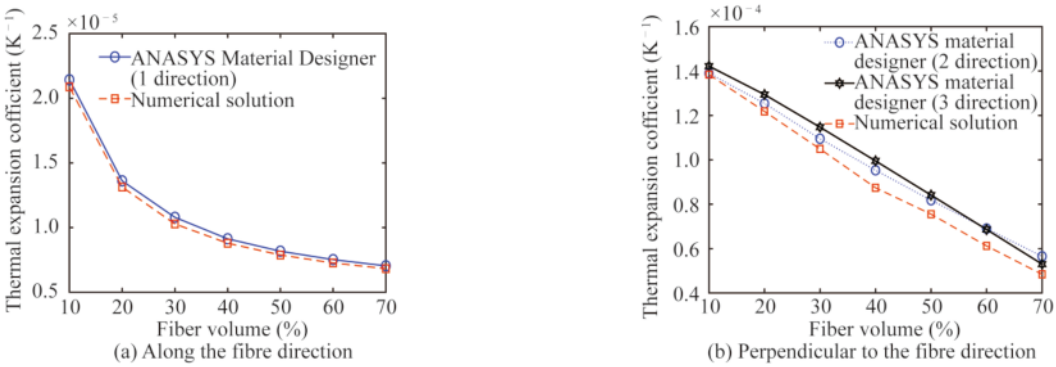

Fig. 5. Comparison results of thermal expansion coefficients.

Fibre tensile pattern ($\sigma_1 > 0$):

$$\left(\frac{\sigma_1}{X_t}\right)^2+\left(\frac{\tau_{12}}{X_{12}}\right)^2+\left(\frac{\tau_{13}}{X_{13}}\right)^2=R_{ft}. \tag{37}$$

Fibre compression pattern ($\sigma_1 < 0$):

$$\left(\frac{\sigma_1}{X_C}\right)^2=R_{fc}. \tag{38}$$

Matrix tensile failure ($\sigma_2 > 0$):

$$\left(\frac{\sigma_2+\sigma_3}{Y_t}\right)^2+\frac{1}{X_{23}^2}\left(\tau_{23}^2-\sigma_2\sigma_3\right)+\left(\frac{\tau_{12}}{X_{12}}\right)^2+\left(\frac{\tau_{13}}{X_{13}}\right)^2=R_{mt}. \tag{39}$$

Matrix compression failure ($\sigma_2 < 0$):

$$\frac{1}{Y_C}\left[\left(\frac{Y_C}{2X_{23}}\right)^2-1\right](\sigma_2+\sigma_3)+\frac{1}{4X_{23}^2}(\sigma_2+\sigma_3)^2+\frac{1}{X_{23}^2}(\tau_{23}^2-\sigma_2\sigma_3)+\left(\frac{\tau_{12}}{X_{12}}\right)^2+\left(\frac{\tau_{13}}{X_{13}}\right)^2=R_{mc}. \tag{40}$$

Fibre matrix shear failure:

$$\left(\frac{\sigma_1}{X_C}\right)^2+\left(\frac{\tau_{12}}{X_{12}}\right)^2+\left(\frac{\tau_{13}}{X_{13}}\right)^2=R_s. \tag{41}$$

Tensile delamination failure ($\sigma_3 > 0$):

$$\left(\frac{\sigma_3}{Z_T}\right)^2+\left(\frac{\tau_{13}}{X_{13}}\right)^2+\left(\frac{\tau_{23}}{X_{23}}\right)^2=R_{td}. \tag{42}$$

Compression delamination failure ($\sigma_3 < 0$):

$$\left(\frac{\sigma_3}{Z_C}\right)^2+\left(\frac{\tau_{13}}{X_{13}}\right)^2+\left(\frac{\tau_{23}}{X_{23}}\right)^2=R_{cd}, \tag{43}$$

where σ_1, σ_2, σ_3, τ_{12}, τ_{13}, and τ_{23} denote the components for normal stress and shear stress along each direction. The failure factor R_i (i = ft, fc, mt, mc, s, td, and cd) represents the damage-induced condition. Damage occurs when the failure factor exceeds 1 (Hashin, 1981).

Special degradation forms (performance-associated parameters) could be realized under the axisymmetric load conditions, as presented in Table 4 (Wang et al., 2021a).

2.4 Numerical analysis procedure

The aforementioned progressive failure model was used with the MATLAB code to study the damage mechanism in RTPs. Successive iterations were performed during the simulation of the relevant loading process. Fig. 6 shows the calculation steps, and iteration and matrix calculation details are presented in the flowchart.

3 Theoretical model validation

3.1 Stress analysis

Damage conditions were assessed to obtain accurate predictions in the stress field. The stress prediction accuracy is important in the progressive failure model for RTPs. Since the difficulty in observing RTP-related stress distribution during the experimental process, numerical simulations were used because it is easy to utilize and is highly efficient in determining the composite stress distribution. For four-layer RTP, commercial software ABAQUS was used for theoretical model verification. Eight-node liner brick elements containing reduced integration (C3D8R) were adopted to simulate the liner, laminate, and coating because of their efficacy in linear and nonlinear problems, including contact, plasticity, and large deformation (Bai et al., 2016; Liu and Wang, 2019b). Reference points RP1 and RP2 were

Table 4 Degradation of performance-related parameters for the composite

		E_{11}	E_{22}	E_{33}	v_{12}	v_{13}	v_{23}	G_{12}	G_{13}	G_{23}
Matrix failure	Tensile	1	0.3	1	1	1	1	0.3	1	0.3
	Compression	1	0.4	1	1	1	1	0.4	1	0.4
Fibre failure	Tensile	0.07	1	1	1	1	1	1	1	1
	Compression	0.14	1	1	1	1	1	1	1	1
Layered failure	Tensile	1	0.3	0.3	1	1	1	1	0.3	0.3
	Compression	1	0.4	0.4	1	1	1	1	0.4	0.4

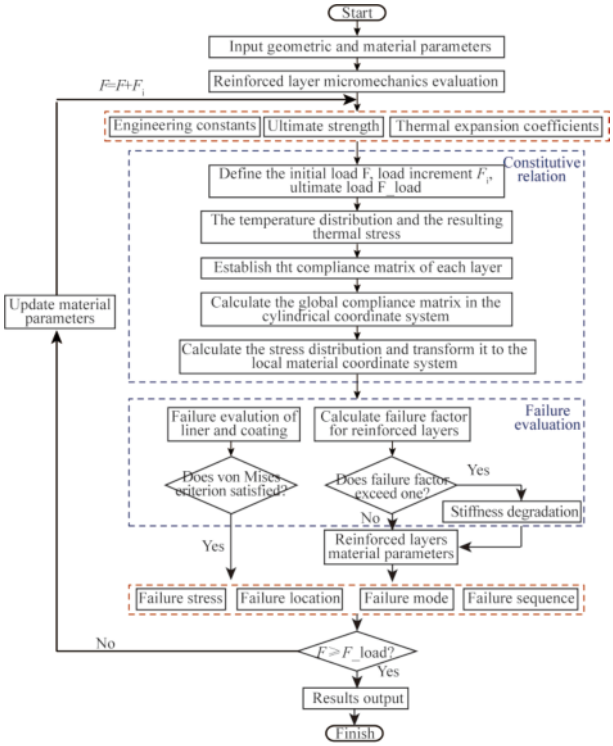

Fig. 6. Flowchart of the calculation procedure.

placed in the central part of two cross-sections, which exhibited kinematic coupling with the nodes of the cross-sections. In particular, RP1 was stationary, whereas RP2 was allowed to move in the longitudinal direction. The internal hydrostatic pressure of 1 MPa was exerted on the RTP inner surface, and the axial tension of 1 kN was used on the reference point RP2. A temperature difference of 1°C (1°C higher than the reference temperature) was added to the whole pipeline. An explicit quasi-static analysis with ABAQUS was performed.

Furthermore, the axial stress $\sigma_z^{(i)}$, radial stress $\sigma_r^{(i)}$, hoop stress $\sigma_\theta^{(i)}$, and shear stress $\tau_{z\theta}^{(i)}$ were used. The analysis results for stress prediction under the analytical model and numerical simulation are shown in Fig. 7.

As indicated by the calculation results presented in Fig. 7, the results of theoretical model-based calculation are consistent with those of numerical simulations, with an error of approximately 5%. Simultaneously, due to different material properties, the bearing capacity and winding angle of each layer of RTPs, the axial stress, hoop stress, and shear stress lead to the stress mutation phenomenon. Thus, the model can effectively provide stress distribution predictions.

3.2 Experimental analysis

To validate the theoretical model and obtain experimental proofs for the theoretical analysis results, three groups of sample pipes were used in the study to investigate the tensile performance of RTPs subject to internal pressure. The structure of the sample pipe, obtained from Weihai Nacheon Pipeline Co., Ltd, is displayed in Fig. 8a. Both the coating and liner comprised HDPE, whereas composite laminates consisted of glass fibre/HDPE tapes. Corresponding winding angles for the neighbouring reinforced layer were 55°/−55° (±55°). The experiment was performed in the closed laboratory of Qingdao Ocean Engineering and Subsea Equipment Inspection & Testing Co., Ltd, which ensured the stability and safety of the experimental environment. Simultaneously, to ensure the stability of internal pressure in the sample pipe during the experiment, a sealed clamping joint was designed.

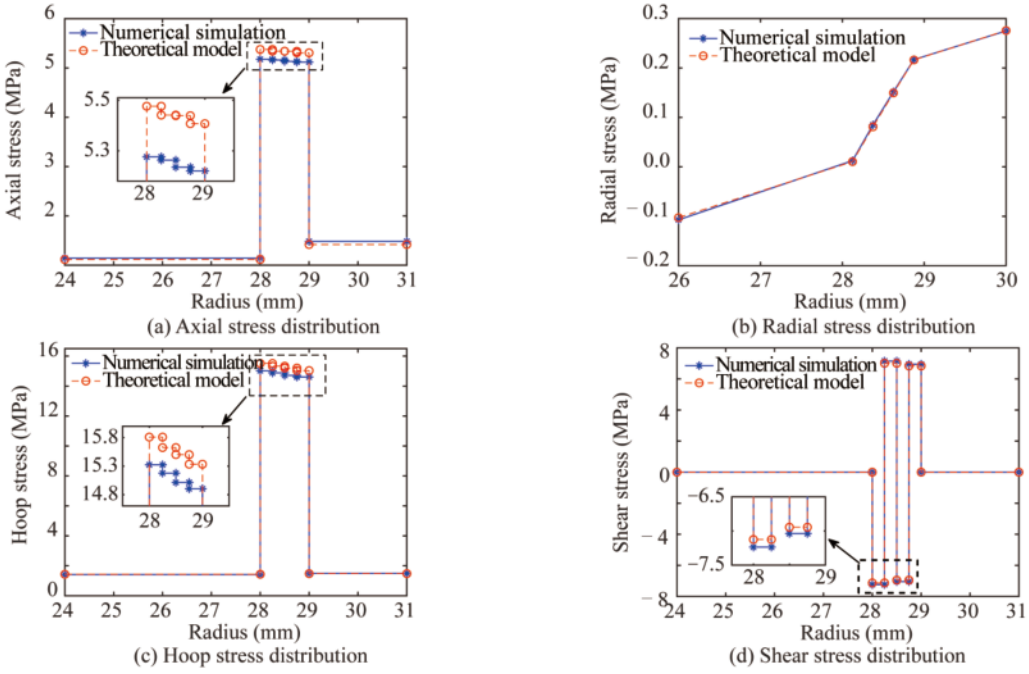

Fig. 7. Stress distribution of the cylindrical coordinate system.

A high-frequency fatigue testing machine (Fig. 8b) was adopted in the experiment, and each sample pipe was loaded using an invariant speed control at the tensile speed of 10 mm/min. Tensile trials were conducted based on ASTM-D2105-01 (ASTM, 2000). The internal hydraulic pressure of 2 MPa was applied to each sample pipe before tensile tests at 22°C. Table 5 presents the geometric parameters of the sample pipes.

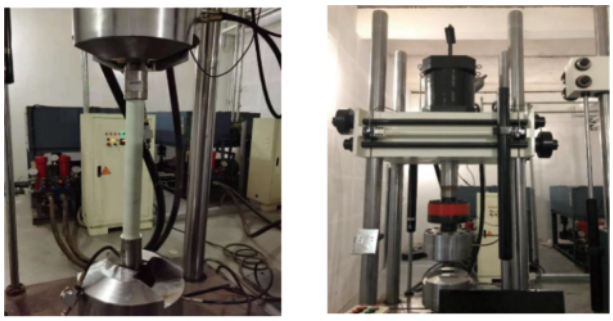

(a) Sample pipe (b) High-frequency fatigue testing machine

Fig. 8. Experimental apparatus.

Table 5 Geometric parameters of the sample pipes

Geometrical parameters	Number of reinforced layers		
	4	12	16
Inner diameter (mm)	48	50	50
Outside diameter (mm)	62	64	66
Inner PE liner thickness (mm)	4.0	4.0	4.0
Reinforced layer thickness (mm)	4×0.25	12×0.25	16×0.25
Protective layer thickness (mm)	2	0	0
Length (mm)	900	900	900
Joint length (mm)	195×2	195×2	195×2

The outer protective layer above the four-layer sample pipe was disassembled. A preliminary test revealed that this layer remained undamaged even when the inner layer and reinforced layers were damaged. Therefore, during the test, the outer protective layer of twelve- and sixteen-layered sample pipes was removed, the fibre-reinforced layer was intact, and the thickness of the protective layer was 0. The tensile load-axial strain relationship of four-, twelve-, and sixteen-layer fibre-wound RTPs was measured using the theoretical model described in Section 2. Relevant RTP parameters used with this theoretical model and experimental parameters were equal. The theoretical and experimental results were studied comparatively. In practice, if the tensile strain in RTPs exceeded 10%, the scenario was invalid (Bai et al., 2014; Lou et al., 2020). Therefore, the results of the experimental measurements and theoretical calculations for strains of smaller than 10% were measured. These results are presented in Fig. 9 and Table 6.

When the axial strain was smaller than 10%, the theoretical results conformed to the experimental results (Fig. 9). A comparison of elastic stiffness is presented in Table 6. For elastic stiffness, the maximum error of the theoretical and experimental results approached 10%. Limited experimental conditions and the mechanical model were considered, which revealed that the differences were in an acceptable range.

4 Stochastic analysis

Different design parameters, such as the pipe diameter, winding angle, fibre volume content, and layer thickness, considerably influence the pipe structure and mechanical performance. To manufacture RTPs, the winding angle and fibre volume content associated with the reinforced tape cannot be constant. The parameters substantially affected mechanical properties, such as elastic modulus, ultimate strength, and thermal expansion coefficients of RTPs. The stochastic analysis has extensive applications in composite laminates. However, limited studies have been conducted for forecasting mechanical properties in RTPs (Rafiee and

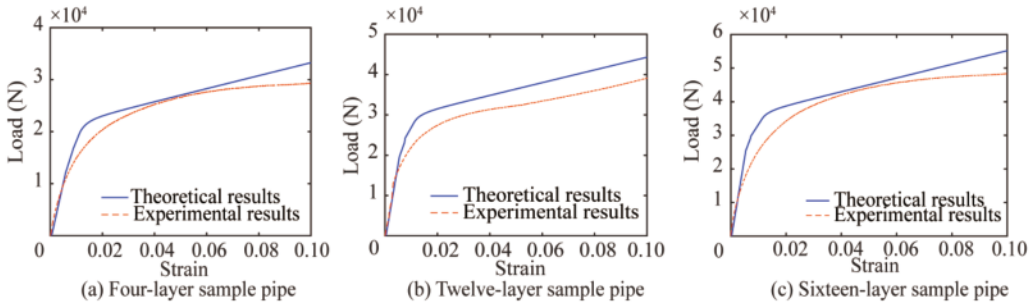

Fig. 9. Comparison of the theoretical results with the corresponding experimentally measured values.

Table 6 Comparison between the theoretical and experimental results

Ply number		4	12	16
Elastic stiffness	Theoretical results (kN)	2258.1	3548.5	4627.1
	Experimental results (kN)	2512.8	3816.3	4171.3
	Differences (%)	11.3	7.5	10.9

Torabi, 2018). Therefore, the fibre volume content and winding angle in the reinforced tape were used as random parameters to study how manufacturing inconsistencies affected tensile properties in RTPs. The internal pressure of all the pipes was 1 MPa; their initial temperature (T_{ref}) was 25°C; their ambient temperature was 25°C; and their fluid temperature was 70°C. Eqs. (19)–(35) (Section 2.2) were adopted to predict the elastic modulus, ultimate strength, and thermal expansion coefficients of the reinforced tape.

4.1 Failure analysis

To analyze the potential failure modes in RTPs, the theoretical model was adopted for calculating the failure modes and failure tensile loads in axial loading. The geometric parameters of RTPs are presented in Table 5. The corresponding material parameters are consistent with the data of Section 2.2. The calculation results are displayed in Table 7.

Table 7 Failure tensile loads of reinforced layers

Ply number	Failure mode					
	Fibre tensile (kN)		Matrix tensile (kN)		Fibre matrix shear (kN)	
	Inner	Outer	Inner	Outer	Inner	Outer
4	12.89	12.94	11.05[1]	11.08	21.79	21.82[2]
12	21.28	21.49	18.84[1]	19.00	29.01	29.05[2]
16	27.22	27.59	24.50[1]	24.61	35.98	36.02[2]

[1] denotes the FPF tensile load; [2] denotes the FF tensile load.

The results presented in Table 7 reveal that FPF is primarily subject to matrix tensile failure. As tensile load increased, matrix tensile failure first emerged from the innermost layer at the reinforced layer. Next, the resulting fibre tensile failure as well as the fibre matrix shear failure resulted in RTP failure. With the failure of the fibre and matrix, the stiffness at the reinforced layer reduced quickly, resulting in fibre matrix shear failure, which led to catastrophic damage to the whole pipeline.

4.2 Stochastic prediction for failure load

From the data provided by the material supplier in Section 2.2, the fibre volume content of the reinforced tape is 40% and the winding angles are 55° and −55° (±55°). With ±2.5° deviation, the winding angles changed between 52.5° and 57.5° (Rafiee and Torabi, 2018). The fibre content fluctuation range (35%–45%) was based on the statistical data provided by the manufacturer. For four-layer RTPs, the failure model presented in Section 2 was randomly enforced with the Monte–Carlo approach (Rafiee et al., 2015a; Rafiee and Torabi, 2018), and the random sampling was performed for the fibre volume content and winding angle (Fig. 10). The coefficient of variation (*CV*) denotes the ratio of standard deviation to the mean, which can be used as a statistical measure to compare the degree of variation from one data series to another, even with the huge difference in the mean values. Therefore, the number of random samples was determined using *CV* of the FPF and FF tensile load prediction. According to the definition of traditional statistical methods, weak variation is defined as $CV \leqslant 0.1$, moderate variation is defined as $0.1 < CV < 1$, and strong variation is defined as $CV \geqslant 1$ (Lei et al., 1988). The convergence trend of *CV* is displayed in Fig. 11, which shows the convergence results of 100 samples.

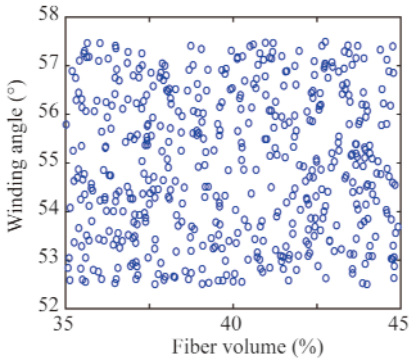

Fig. 10. Random sample distribution.

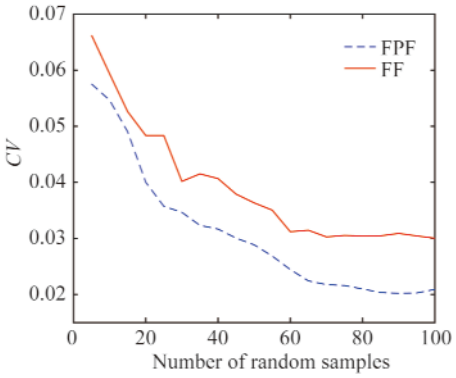

Fig. 11. Convergence trend of *CV*.

According to Fig. 11, the results converged after the generation of the 100 samples, and the *CV* value was smaller than 0.1. Therefore, the 100 samples were generated for the random analysis. By comparing *CV* (Fig. 11), when the number of random samples reached 100, *CV* of the FPF tensile load stabilized at approximately 0.03, and that of the FF tensile load stabilized at approximately 0.02. Therefore, the influence of parameter randomness on the FPF tensile load was considerably less than that of the FF tensile load. To explore how random parameters affected the failure tensile load, the FPF and FF tensile load histograms were obtained for random analysis (Fig. 12). The calculation results are shown using the Weibull probability density distribution (Fig. 13).

According to the calculation results presented in Figs. 12 and 13, in consideration of randomness in various parameters, the failure tensile load of RTPs fluctuated within a certain range. Based on Weibull probability density distribution (Fig. 13), the probability to obtain a value of the FPF tensile load below the average was 0.575. For the FF

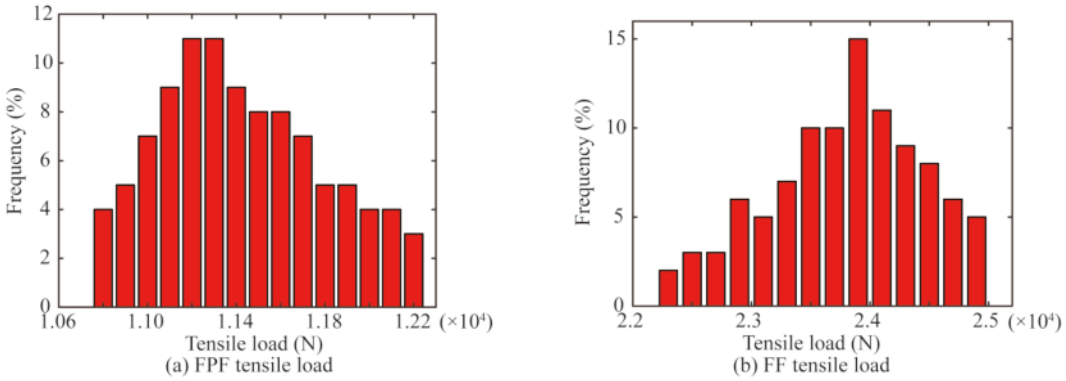

Fig. 12. Tensile load histogram predicted in the stochastic analysis.

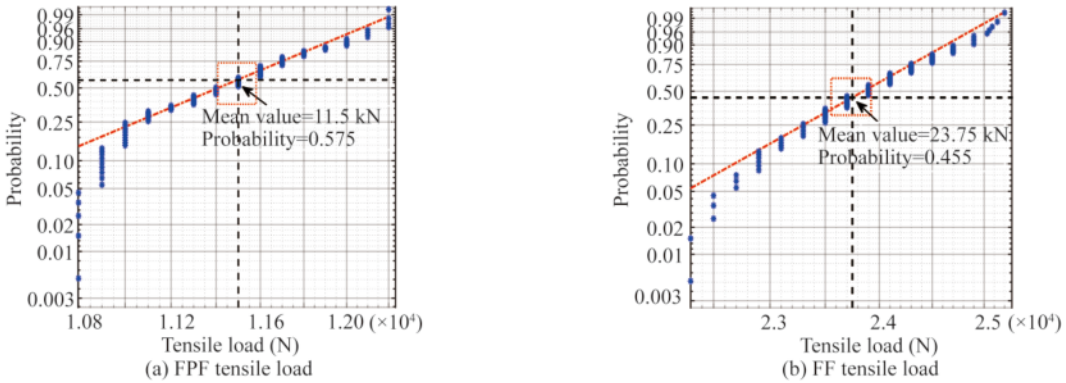

Fig. 13. Weibull probability distribution for FPF and FF tensile loads.

tensile load, the probability was 0.455 lower than the mean value. In consideration of randomness in production parameters, a certain probability that both the FPF and FF tensile loads were lower than the mean value and that the FPF tensile load exhibited a higher probability to be lower than the average exceeded 0.5. Hence, in the manufacturing process, manufacturing parameter adjustment and prudent monitoring for consistency in the production system can maximize the load-bearing ability for the manufactured RTPs.

4.3 Random variable study

This study explored how a single variable affected FPF and FF tensile loads. First, the fibre content in the reinforced tape was a random variable, and the winding angle in the reinforced tape was maintained constant at ±55°. Next, the winding angle in the reinforced tape was a random parameter, whereas the fibre content was maintained constant at 40%. Standard deviation (*SD*) was considered a statistical measure for dataset dispersion relative to the mean. In this section, *SD* was used to calculate the dispersion degree of the failure tensile load influenced by different random parameters. Figs. 14–16 display the calculation results.

The calculation results were comparatively studied to examine the dispersion degree for FPF and FF tensile loads with different random variables. Table 8 presents the calculation results.

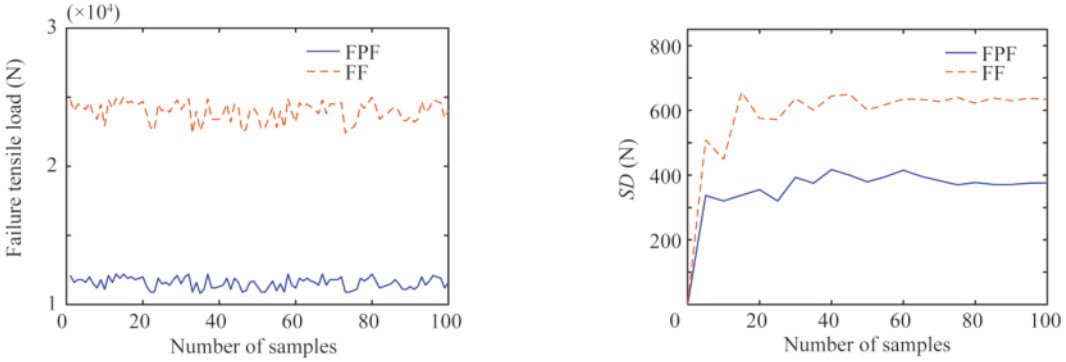

Fig. 14. Failure tensile load and *SD* under the random fibre volume content assumption.

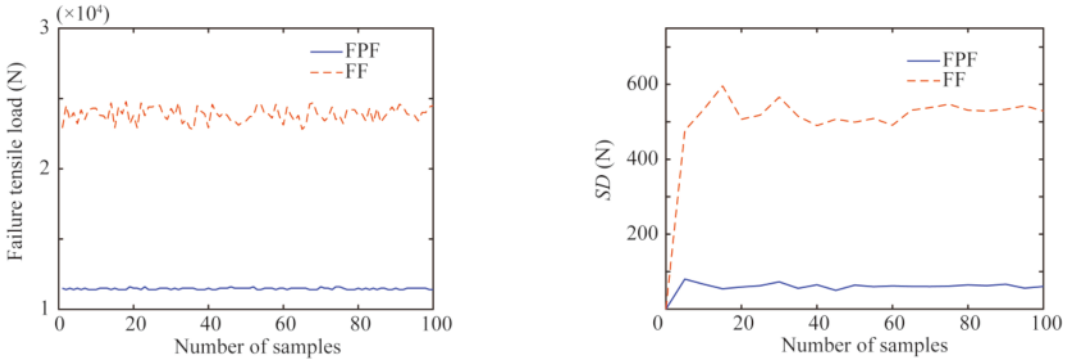

Fig. 15. Failure tensile load and *SD* under the random winding angle assumption.

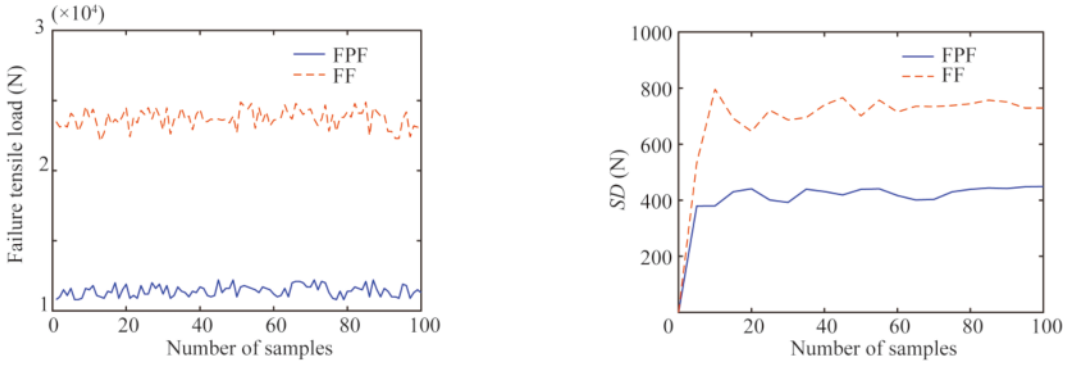

Fig. 16. Failure tensile load and *SD* under multiple random parameters.

Table 8 Estimated FPF and FF tensile load and *SD* values under various random variables

Random variable	FPF tensile load (kN)				FF tensile load (kN)			
	Mean value	Min.	Max.	*SD*[1]	Mean value	Min.	Max.	*SD*[1]
Fibre content	11.5	10.8	12.2	0.41	23.8	22.6	24.9	0.63
Winding angle	11.5	11.4	11.6	0.06	23.8	22.8	24.8	0.53
Combined variable	11.5	10.8	12.2	0.45	23.8	22.3	25.2	0.75

[1] denotes the *SD* for 100 samples.

Based on the statistics of Table 8, influenced by random parameters, the average FPF tensile load was maintained constant at approximately 11.5 kN, and the average FF tensile load was 23.8 kN. The results revealed that parameter randomness had a negligible effect on averages. Under the combined variable condition, the gap between the maximum and minimum failure tensile loads peaked, with the highest dispersion degree. Further analyses indicated the randomness of the fibre content as the major factor controlling the fluctuation of the FPF tensile load, and the winding angle at the reinforced layer seldom affected the fluctuation in the FPF tensile load. For the FF tensile load, the fibre content and winding angle exhibited obvious effects. The failure tensile load of 6-, 8-, 10- and 12-layer RTPs was measured for analyses, and *SD* of the failure tensile load with different random variables was summarized (Fig. 17).

The calculation results (Fig. 17) showed the *SD* value, and the fluctuation scope for the failure tensile load progressively increased with an increase in the ply number at the reinforced layer in RTPs. Practical applications for RTPs require multiple plies at the reinforced layer for protection against the harsh marine environment. Therefore, the inconsistencies of production parameters were strictly controlled. Fig. 17a proves the insignificant impacts of the winding angle on the FPF tensile load and that the fluctuation of the FPF tensile load was mainly controlled by using the fibre content. According to Fig. 17b, the randomness of the fibre content exerted insignificant effects on the winding angle for the FF tensile load.

5 Conclusions

This study provided a stochastic tensile failure assessment of RTPs subject to axial loading and internal pressure with analytical, experimental, and numerical approaches. The stress distribution of RTPs was under axial loading and the internal pressure was studied with 3D elasticity theory, and the analytical micromechanics of composites was evaluated. By considering the effect of temperature, the 3D Hashin–

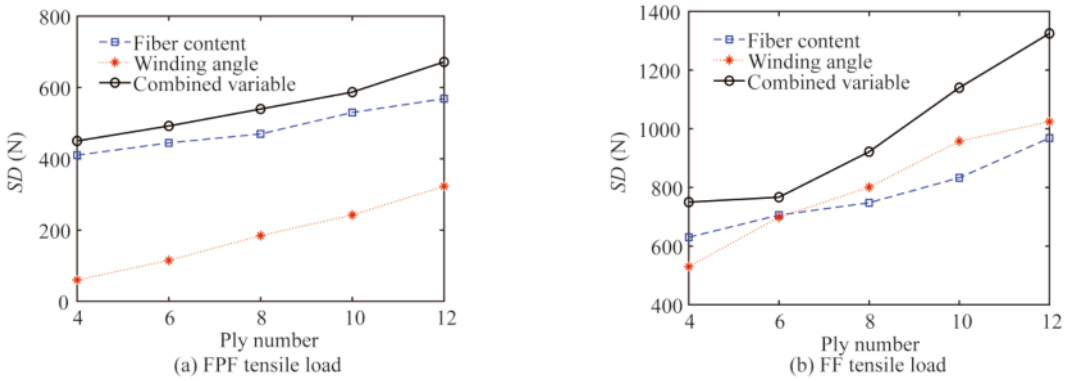

Fig. 17. *SD* values in 100 samples of 4, 6, 8, 10, and 12-layer RTPs.

Yeh failure criterion was combined with the damage evolution model to construct the progressive failure model. Theoretical model-derived results were verified by using the explicit quasi-static analysis through ABAQUS and experiments. The comparison revealed that the progressive failure model exhibited the same trends with the finite element method and experimental results. Moreover, the model can calculate the stress distribution, identify failure modes, predict failure sequences, and evaluate the ultimate tensile load of RTPs.

In consideration of the parameter randomness of the fibre content and winding angle at the reinforced layer, the Monte–Carlo approach was adopted to generate adequate samples. The random analysis was performed on tensile failure load with a progressive failure model featuring iteration and cycling, and the stochastic analysis results were statistically assessed by the Weibull probability density distribution function. The thermal expansion coefficients and ultimate strength of the reinforced tape under the influence of the fibre volume content were used as random parameters.

The influence of producing inconsistencies in the tensile properties in RTPs was studied with the random analysis method. The results demonstrated that FPF is primarily subject to matrix tensile failure, whereas FF is subject to fibre matrix shear failure. In consideration of the randomness under different parameters, a certain probability exists that the tensile loads of FPF and FF are lower than the mean values, which increases the probability to obtain a lower value for the FPF tensile load than the mean value. The randomness of parameters rarely affects the average of the failure tensile load. The randomness of the fibre content is the main factor controlling the fluctuation of the FPF tensile load, and the fibre content and winding angle exert the same effect on the FF tensile load. As the ply number at RTP-reinforced layers increases, the fluctuation range of failure tensile load gradually increases. Therefore, the inconsistencies in production parameters should be strictly controlled.

References

ASTM, 2000. *Standard Test Method for Longitudinal Tensile Properties of "Fiberglass" (Glass-Fiber-Reinforced Thermosetting-Resin) Pipe and Tube*.

Bai, Q. and Bai, Y., 2014. 27-Burst strength of RTP pipeline, in: Bai, Q. and Bai, Y. (eds.), *Subsea Pipeline Design, Analysis, and Installation*, Gulf Professional Publishing, Tokyo, pp. 611–620.

Bai, Y., Liu, T., Cheng, P., Yuan, S., Yao, D.Z. and Tang, G., 2016. Buckling stability of steel strip reinforced thermoplastic pipe subjected to external pressure, *Composite Structures*, 152, 528–537.

Bai, Y., Tang, J.D., Xu, W.P., Cao, Y. and Wang, R.S., 2015. Collapse of reinforced thermoplastic pipe (RTP) under combined external pressure and bending moment, *Ocean Engineering*, 94, 10–18.

Bai, Y., Xu, W.P., Cheng, P., Wang, N.S. and Ruan, W.D., 2014. Behaviour of reinforced thermoplastic pipe (RTP) under combined external pressure and tension, *Ships and Offshore Structures*, 9(4), 464–474.

Bakaiyan, H., Hosseini, H. and Ameri, E., 2009. Analysis of multi-layered filament-wound composite pipes under combined internal pressure and thermomechanical loading with thermal variations, *Composite Structures*, 88(4), 532–541.

Bakar, M.A.A., Mustaffa, Z., Idris, N.N. and Ben Seghier, M.E.A., 2021. Experimental program on the burst capacity of reinforced thermoplastic pipe (RTP) under impact of quasi-static lateral load, *Engineering Failure Analysis*, 128, 105626.

Betts, D., Sadeghian, P. and Fam, A., 2019. Investigation of the stress-strain constitutive behavior of ±55° filament wound GFRP pipes in compression and tension, *Composites Part B*: *Engineering*, 172, 243–252.

Chen, Y., Fu, K.K., Hou, S.J., Han, X. and Ye, L., 2018. Multi-objective optimization for designing a composite sandwich structure under normal and 45° impact loadings, *Composites Part B*: *Engineering*, 142, 159–170.

Chen, Y., Hou, S.J., Fu, K.K., Han, X. and Ye, L., 2017. Low-velocity impact response of composite sandwich structures: modelling and experiment, *Composite Structures*, 168, 322–334.

Davydenko, V.I., 1970. Strength and deformability of reinforced polymers in tension normal to the fibers, *Polymer Mechanics*, 6(4), 595–599.

Gemi, L., 2018. Investigation of the effect of stacking sequence on low velocity impact response and damage formation in hybrid composite pipes under internal pressure. A comparative study, *Composites Part B*: *Engineering*, 153, 217–232.

Hashin, Z., 1981. Fatigue failure criteria for unidirectional fiber composites, *Journal of Applied Mechanics*, 48(4), 846–852.

Hashin, Z. and Rotem, A., 1973. A fatigue failure criterion for fiber reinforced materials, *Journal of Composite Materials*, 7(4), 448–464.

Hastie, J.C., Guz, I.A. and Kashtalyan, M., 2019. Effects of thermal gradient on failure of a thermoplastic composite pipe (TCP) riser leg, *International Journal of Pressure Vessels and Piping*, 172, 90–99.

He, W.T., Yao, L., Meng, X.J., Sun, G.Y., Xie, D. and Liu, J.X., 2019. Effect of structural parameters on low-velocity impact behavior of aluminum honeycomb sandwich structures with CFRP face sheets, *Thin-Walled Structures*, 137, 411–432.

Lei, Z.D., Yang, S.X., and Xie, S.Z., 1988. *Soil Water Dynamics*. Tsinghua University Press, Beijing. (in Chinese)

Liu, W.C. and Wang, S.Q., 2019a. Analytical prediction of buckling collapse for reinforced thermoplastic pipes based on hoop stress analysis of crushed rings, *Ocean Engineering*, 187, 106203.

Liu, W.C. and Wang, S.Q., 2019b. An elastic stability-based method to predict the homogenized hoop elastic moduli of reinforced thermoplastic pipes (RTPs), *Composite Structures*, 230, 111560.

Liu, W.C., Wang, S.Q., Bu, J.R. and Ding, X.D., 2021a. An analytical model for the progressive failure prediction of reinforced thermoplastic pipes under axial compression, *Polymer Composites*, 42(6), 3011–3024.

Liu, W.C., Wang, S.Q., Wang, S. and Ci, S.Z., 2021b. Theoretical and experimental study on the continuum damage mechanical (CDM) behavior of RTPs under axial tension, *Ocean Engineering*, 222, 108623.

Lou, M., Wang, Y.Y., Tong, B. and Wang, S., 2020. Effect of temperature on tensile properties of reinforced thermoplastic pipes, *Composite Structures*, 241, 112119.

Maimí, P., Camanho, P.P., Mayugo, J.A. and Dávila, C.G., 2007. A continuum damage model for composite laminates: Part I–Constitutive model, *Mechanics of Materials*, 39(10), 897–908.

Rafiee, R., 2013. Experimental and theoretical investigations on the failure of filament wound GRP pipes, *Composites Part B*: *Engineering*, 45(1), 257–267.

Rafiee, R. and Amini, A., 2015. Modeling and experimental evaluation of functional failure pressures in glass fiber reinforced polyester pipes, *Computational Materials Science*, 96, 579–588.

Rafiee, R., Fakoor, M. and Hesamsadat, H., 2015a. The influence of production inconsistencies on the functional failure of GRP pipes, *Steel and Composite Structures*, 19(6), 1369–1379.

Rafiee, R., Reshadi, F. and Eidi, S., 2015b. Stochastic analysis of functional failure pressures in glass fiber reinforced polyester pipes, *Materials & Design*, 67, 422–427.

Rafiee, R. and Torabi, M.A., 2018. Stochastic prediction of burst pressure in composite pressure vessels, *Composite Structures*, 185, 573–583.

Reis, J.M.L., Martins, F.D.F. and da Costa Mattos, H.S., 2017. Influence of ageing in the failure pressure of a GFRP pipe used in oil industry, *Engineering Failure Analysis*, 71, 120–130.

Shen, G.L., Hu, G.K. and Liu, B., 2013. *Mechanics of Composite Materials*, Second ed., Tsinghua University Press, Beijing, China. (in Chinese)

Sun, X.S., Chen, Y., Tan, V.B.C., Jaiman, R.K. and Tay, T.E., 2014a. Homogenization and stress analysis of multilayered composite offshore production risers, *Journal of Applied Mechanics*, 81(3), 031003.

Sun, X.S., Tan, V.B.C., Chen, Y., Tan, L.B., Jaiman, R.K. and Tay, T. E., 2014b. Stress analysis of multi-layered hollow anisotropic composite cylindrical structures using the homogenization method, *Acta Mechanica*, 225(6), 1649–1672.

Toh, W., Tan, L.B., Tse, K.M., Giam, A., Raju, K., Lee, H.P. and Tan, V.B.C., 2018. Material characterization of filament-wound composite pipes, *Composite Structures*, 206, 474–483.

Wang, Y.Y., Lou, M., Dong, W.Y. and Wang, Y., 2021a. Predicting failure pressure of reinforced thermoplastic pipes based on theoretical analysis and experiment, *Composite Structures*, 270, 114039.

Wang, Y.Y., Lou, M., Tong, B. and Wang, S., 2020. Mechanical properties study of reinforced thermoplastic pipes under a tensile load, *China Ocean Engineering*, 34(6), 806–816.

Wang, Y.Y., Lou, M., Zeng, X., Dong, W.Y. and Wang, S., 2021b. Burst capacity of reinforced thermoplastic pipes based on progressive failure criterion, *Ocean Engineering*, 234, 109001.

Xin, H.H., Mosallam, A., Liu, Y.Q., Veljkovic, M. and He, J., 2019. Mechanical characterization of a unidirectional pultruded composite lamina using micromechanics and numerical homogenization, *Construction and Building Materials*, 216, 101–118.

Xing, J.Z., Geng, P. and Yang, T., 2015. Stress and deformation of multiple winding angle hybrid filament-wound thick cylinder under axial loading and internal and external pressure, *Composite Structures*, 131, 868–877.

Yeh, H.Y. and Chern, C., 1998. The Yeh-Stratton criterion for stress concentrations in fiber-reinforced composite materials, *Journal of Composite Materials*, 32(2), 141–157.

Yeh, H.Y. and Kim, C.H., 1994. The Yeh-Stratton criterion for composite materials, *Journal of Composite Materials*, 28(10), 926–939.

Yu, K., Morozov, E.V., Ashraf, M.A. and Shankar, K., 2017. A review of the design and analysis of reinforced thermoplastic pipes for offshore applications, *Journal of Reinforced Plastics and Composites*, 36(20), 1514–1530.